AUT Journal of Electrical Engineering
10.22060/EEJ.2026.25667.5989

A Half Hexagonal Fractal L-Band Antenna with SAR Analysis for Wearable Application.

Atul Rupchandra Chaudhari[1*], Dipak Pandurang Patil[2]

[1] Research Scholar,
[1]Sandip Institute of Technology and Research Centre, Nashik, 422213, India.
[1,2]Savitribai Phule Pune University, Pune, India.

[2]Sandip Institute of Engineering and Management, Nashik, 422213, India.

*Corresponding author: ar.chaudhari1@gmail.com

Abstract

This paper presents the design, comprehensive analysis, and experimental validation of a flexible, wearable antenna optimized for operation in the L-band frequency spectrum. The proposed antenna utilizes a coplanar waveguide (CPW) feeding structure and is realized on the polyethylene substrate characterized by a dielectric constant of 2.5 and a thickness of 1.5 mm. With compact dimensions of, 90 x 144 x 1.5 mm^3, the antenna offers excellent mechanical flexibility, low profile, and high radiation efficiency, making it ideally suitable for integration in 1.6 GHz L-band for precise and robust navigation performance. Electromagnetic simulations and prototype measurements confirm broadband impedance matching, consistent radiation patterns, and stable gain performance under various bending radii, ensures mechanical robustness and electromagnetic reliability in dynamic on-body conditions. To assess user safety and electromagnetic exposure, a specific absorption rate (SAR) analysis is performed using a three-layer human tissue-equivalent phantom for both 1-gram and 10-gram tissue masses. Evaluations are conducted across multiple proximity scenarios, including direct skin contact and spatial offsets of 1 mm, 3 mm, and 5 mm from the body surface. The observed SAR values comply with international safety standards, remaining below the regulatory thresholds of 1.6 W/kg (IEEE) and 2.0 W/kg (ICNIRP), thereby confirming the antenna's viability for safe and reliable use in wearable biomedical applications.

Keywords: Specific absorption rate, Wearable, Flexible, Half hexagon, L- band

1. Introduction

The L-band, spanning from 1 GHz to 2 GHz, is a critical segment of the radio frequency spectrum used in a variety of wireless communication and sensing applications. The corresponding wavelength ranges from 30 cm (1 GHz) to 15 cm (2 GHz), which enables the development of moderately compact antenna designs. The lower portion of the band, particularly around 1.5 GHz, offers longer communication ranges, making it ideal for satellite systems such as Inmarsat, which operate over several hundred to several thousand kilometres [1]. One of the key advantages of L-band frequencies is their strong penetration capability, enabling effective communication in non-line-of-sight (NLOS) environments, such as through vegetation, urban infrastructure, or during adverse weather conditions. Additionally, L-band signals exhibit low atmospheric attenuation and reduced susceptibility to multipath interference, ensuring reliable performance in complex environments. The relatively short wavelength also supports the development of compact antennas, facilitating their integration into mobile, wearable, and portable devices [2]. In wearable technologies, particularly in health monitoring or wireless body area networks (WBANs), L-band antennas are effective because they offer a balance between compact size, reliable

Uncorrected Proof

signal strength, and minimal energy absorption by the body, which is crucial for user safety. Since the L-band operates in the lower frequency range, it avoids the higher power requirements and potential health concerns associated with higher frequency bands [3].

The systems operating in this band, including GPS, satellite phones, and aviation communication, benefit from global coverage and robust signal propagation. However, the L band does have limitations, including restricted bandwidth, which can limit achievable data rates compared to higher frequency bands. Despite this, the L band remains indispensable in fields such as military communications, remote sensing, aviation, maritime navigation, weather radar, and radio astronomy, where reliability, coverage, and signal penetration are more critical than bandwidth [4-5]. The design of wearable antennas relies on a thorough understanding of the electromagnetic properties of materials, as these characteristics directly influence the antenna's performance. Key factors include permittivity, loss tangent, and substrate thickness. Wearable materials are broadly classified into nonconductive textiles and conductive textiles (electro-textiles). Nonconductive textiles are commonly used to minimize the weight and profile of antennas, with materials such as felt, silk, nylon, leather, washed cotton, denim, polymer, fleece, and paper serving as substrates. Additionally, low-dielectric-constant materials like jeans and polyethylene terephthalate (PET) are widely chosen for wearable antenna applications. Conductive textiles (e-textiles) are created by embedding conductive metal or polymer threads into standard fabrics. Examples include Flectron, Zelt, pure copper, taffeta, and Shieldlt, which offer flexibility and durability, making them suitable for body-worn applications [6-7]. These materials are engineered to maintain low and stable electrical resistance, reducing losses and enhancing antenna efficiency. For optimal antenna performance, the substrate must be lightweight and flexible. Additionally, it is crucial to ensure that the antenna does not pose any risks to human health. Since textiles generally have low dielectric constants, they help in minimizing surface wave losses and expand impedance bandwidth, which is beneficial for wearable antennas. One of the primary challenges of body-worn antennas is maintaining consistent performance despite environmental factors such as humidity, temperature variations, proximity to the human body, and repeated washing cycles. Moreover, when multiple wearable antennas or sensors are deployed in a system, their placement and spacing play a critical role in optimizing performance [8-11]. A common method to achieve broadband performance in microstrip antennas (MSAs) is by employing a thicker substrate with a low dielectric constant. This type of substrate lowers the cavity's quality factor beneath the patch, resulting in an increased bandwidth (BW) [12, 13]. Another widely adopted approach to enhance bandwidth is by introducing slots, such as U-shaped, V-shaped, or rectangular slots at specific locations on the patch. These slots generate additional resonant modes close to the fundamental resonant frequency; thereby improving the overall bandwidth. The slot length is typically designed to be a half or quarter wavelength for operation in the intended frequency band [14–16]. The study in [17] is presented for L band at 1.9 GHz for the GPS applications using 3 different substrates such as FR-4, Arlon AD320 and vacuum (air) for the dimension of 100 mm x 100 mm. The author proposed higher value of gain at air. Author [18] implemented design of small size broadband patch antenna at the frequency of 1.63 GHz for L band applications. Six slots have been etched at the ground plane to enhance gain and bandwidth of the antenna. The study in [19] focuses on developing a cost-effective primary surveillance radar (PSR) antenna that operates efficiently in the L-band frequency range (1.3 GHz) using microstrip antenna technology with FR4 substrate material. Author [20] has implemented electromagnetically coupled patch antenna using air gap filled substrate with FDTD method. Broadband stacked microstrip patch antenna for L-Band operation around 1.3 GHz is designed for the improvement in bandwidth.

Thus, many authors significantly contributed in the various application of L band in the range of 1-2 GHz with variation in the use of substrate material. The proposed antenna is making use of light weight foam with very low dielectric constant as substrate to address the issues of narrower bandwidth, improves radiation efficiency and significantly reduces body-loading effects compared to many reported textile and rigid-substrate antennas in the L band operation and wearable applications. Apart

Uncorrected Proof

from these, the main contribution lies in the size reduction for low frequency operation using fractal technique and validation by means of conformal analysis, On-body and SAR analysis. The entire article is structured in different sections as follows with the introduction part in section 1. The methodology and experimental work are presented in Section 2, section 3 presents the equivalent circuit model & analysis, section 4 describes the comparison of results obtained in simulated and actual measured scenario. Also, the bending, on-body and SAR analysis is incorporated in section 5, 6 and 7 respectively. The article is summarized with the noticeable results in section 8.

2. Method and Experimental Work

The antenna is firstly designed with the help of full hexagon considering the side length of 73 mm with the help of Eqs. (1) to (4) stated in [21] and shown in Fig. 1(a). The resonating frequency targeted to 1.5 GHz as the centre of L-band. The antenna geometry is incorporated using a coplanar waveguide (CPW) structure instead of regular grounding method considering wearable application of the design. Whereas, Fig. 1 (b) gives idea about the front view of the antenna highlighting CPW structure with the ground itself on the top side adjacent to patch and feedline by providing gap between them. The results obtained for stage 0 are tabulated in Table 3.

$$f_r = \frac{1.8412C}{2\pi r_e \sqrt{\varepsilon_r}} \tag{1}$$

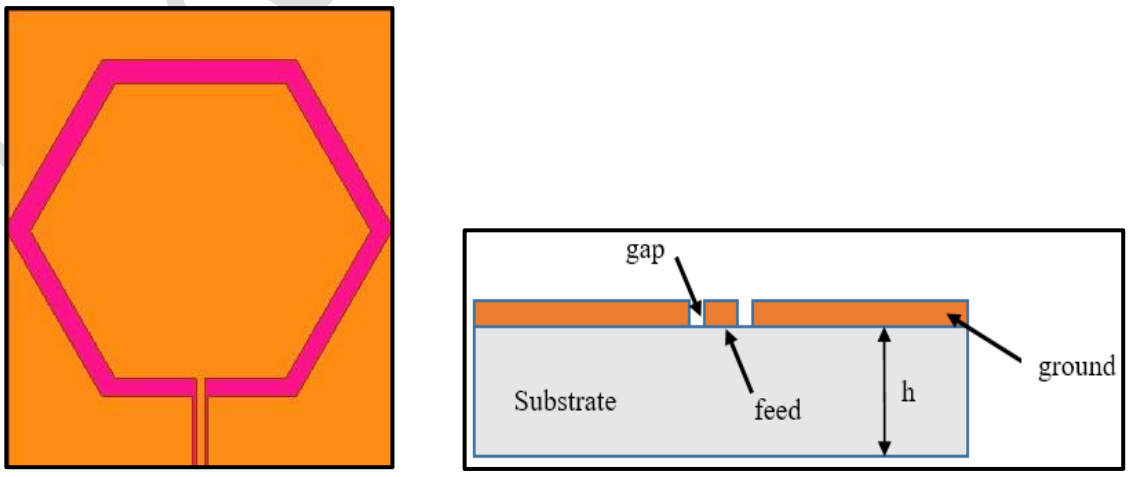
Where r_e is given as;

$$r_e = a\sqrt{\frac{3\sqrt{3}}{2\pi}} \tag{2}$$

and calculated by equating the Eqs. (3) and (4) as stated below;

$$A_{hex} = \frac{3\sqrt{3}}{2}a^2 \tag{3}$$

$$A_{circle} = \pi r_e^2 \tag{4}$$



(a) (b)

Uncorrected Proof

Fig. 1. Basic Geometry (a) Full hexagon structure with CPW (b) Front view of CPW

The antenna design is further advanced by embedding a hexagonal slot within the radiating element, as shown in Fig. 2, with corresponding dimensions listed in Table 1. This geometric enhancement is purposefully optimized to expand the antenna's bandwidth while maintaining compactness. As a result, the modified structure exhibits a broader frequency response along with a more defined and sharper resonance at the desired 1.5 GHz centre frequency. This improvement is accompanied by enhanced impedance matching, clearly illustrated in Fig. 5 and detailed in Table 3. The refined design effectively elevates the antenna's performance, reinforcing its suitability for high-efficiency wearable communication applications.

Table 1. Design Parameters

Parameter	L_{sub}	W_{sub}	W_1	W_2	W_3	L_f	W_f	d	S	W_g
Unit (mm)	173	144	73	66	49	33	3	1.5	6	69

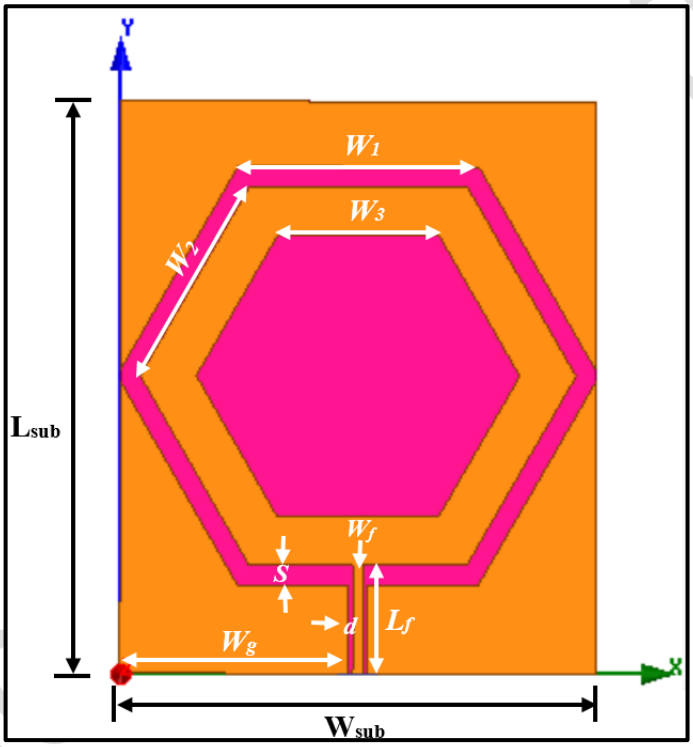


Fig. 2. Modified Geometry as stage 1

The results obtained in Stage 1 demonstrate the effectiveness of the full hexagonal geometry incorporating a central hexagonal slot. However, the major limitation of this design is its relatively large overall dimension of 90 x 144 x 1.5 mm^3, which makes it less suitable for wearable applications. The large size can affect portability, ease of placement, and comfortable integration with different parts of the human body. Therefore, to achieve a more compact and wearable design, the length of the original full-hexagonal geometry is reduced by half, resulting in a half-hexagonal configuration [21], as shown in Fig. 3. This modification significantly reduces the antenna size while retaining the desired electromagnetic characteristics, thereby improving its suitability for wearable applications. This

Uncorrected Proof

10.22060/EEJ.2026.25667.5989

modification aims to maintain performance while significantly improving wearability and integration potential.

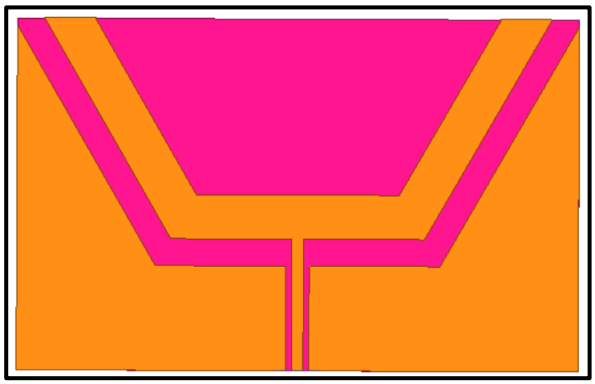


Fig. 3. Half hexagonal geometry as Stage 2

When the antenna's length was reduced to half of its original size, a noticeable shift in the resonant frequency was observed, accompanied by poor impedance matching. This resulted in degraded performance, with lower S_{11} values and a significantly reduced bandwidth. The performance metrics for this configuration, referred to as Stage 2, are summarized in Table 3. Unfortunately, the outcomes of Stage 2 fell short of expectations in terms of key antenna parameters such as reflection coefficient and operational bandwidth. To address these limitations, a fractal design approach was introduced in Stage 3. This technique leverages the principle of self-similarity, where smaller copies of the geometry are recursively embedded within the structure, as illustrated in Fig. 4. The dimensions used to implement this fractal geometry are listed in Table 2. This innovative approach significantly enhanced the antenna's performance, achieving excellent impedance matching with an S_{11} of -41.25 dB and a substantially wider bandwidth of 383 MHz. Most notably, Stage 3 delivered a well-defined resonance precisely at 1.6 GHz, fulfilling the desired performance criteria. The corresponding response is illustrated in Fig. 5 with detailed results in Table 3.

Table 2. Half Hexagon Design Parameters

Parameter	$L_{sub}/2$	W_{sub}	S_1	S_2	t_1	t_2	L_f	W_f	d	W_g	$L_g/2$
Unit (mm)	90	144	7	13.85	11.25	9.6	33	3	1.5	69	88.26

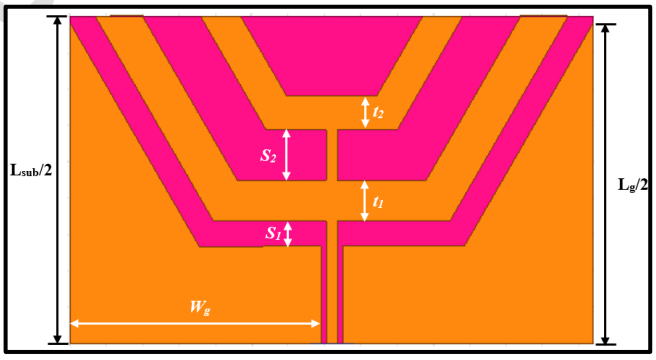


Fig. 4. Fractal Based Half Hexagonal Geometry Stage 3

Uncorrected Proof

10.22060/EEJ.2026.25667.5989

Fig. 5 illustrates the evolution of a CPW-fed antenna through four design stages (Stage 0 to Stage III), highlighting their respective return loss (S_{11}) characteristics across the L-band frequency range (1–2 GHz). Initially, Stage 0 features a simple hexagonal ring structure, which exhibits weak resonance and poor impedance matching, indicated by a shallow dip near 1.6 GHz. In Stage I, the introduction of a central patch enhances coupling, resulting in improved matching. Stage II further modifies the geometry by reducing hexagonal structure to half of its size, leading to deeper resonance due to enhanced capacitive effects. Finally, Stage III incorporates a more intricate, nested layout, significantly refining current distribution and achieving a sharp, deep resonance around 1.6 GHz with S_{11} below –41.25dB. This progressive structural optimization demonstrates how introducing geometric complexity improves electromagnetic coupling and impedance matching, making the final design well-suited for efficient and reliable L-band wireless communication.

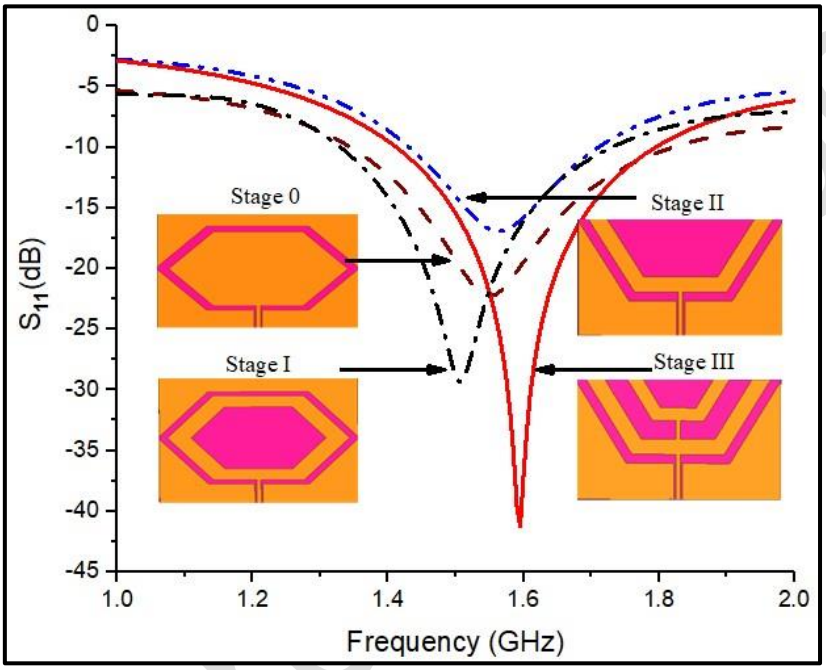


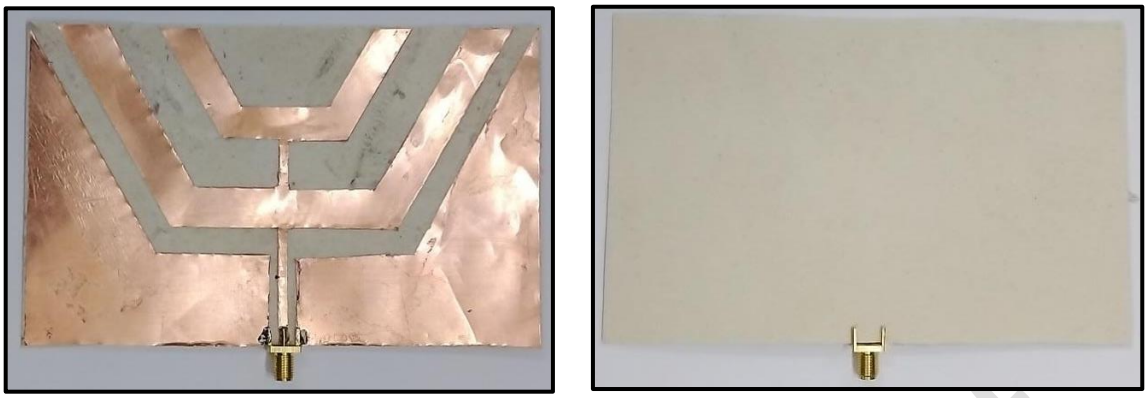
Fig. 5. Return Loss (S_{11}) Performance with Geometry Stages

Table 3. Parametric Study of the Half Hexagonal Shaped Antenna

Parameter/ Geometry	Resonating at (GHz)	Bandwidth (MHz)	S_{11} (dB)
Stage 0	1.55	1.344 - 1.820 (476)	-22.5
Stage I	1.5	1.324 – 1.728(404)	-29.24
Stage II	1.56	1.432 – 1.709 (277)	-16.94
Stage III	1.6	1.412 – 1.795 (383)	-41.25

The results of the stage III are taken into account for the fabrication of prototype. A copper foil of 50 microns is used as a conducting material for patch and the ground plane [22] along with polyethylene substrate of 1.5 mm thickness and dielectric constant of 2.5. A fabricated prototype with top and bottom view in Figs. 6 (a) and (b) is presented respectively with incorporation of CPW technique.

Uncorrected Proof



(a) Top view **(b) Bottom view**

Fig. 6. Fabricated Prototype of the Proposed Work

3. Equivalent Circuit Analysis

A lumped equivalent circuit model of the suggested antenna is constructed and is depicted in Fig. 7. Additionally, this layout is verified by circuit theory analysis, using advanced design system (ADS). Fig. 8. shows the return loss curves for the lumped circuit model. In general, the microstrip patch antenna is comparable to an open-ended transmission line. The lumped equivalent circuit of the proposed CPW-fed fractal antenna is developed using transmission line model by decomposing the antenna geometry into short transmission line sections. Each section is represented by distributed resistance, inductance, capacitance, and conductance parameters. Straight conductor sections are modelled as series inductance and resistance. The input part of the equivalent circuit shows the CPW feed and it works with the radiating structure, and carries current and modelled as an inductor *L1*, resistor *R1* shows the total loss of radiation and conduction at the feed region, the capacitance in the feed region due to the electric field formed between the feed strip and the two symmetrical ground planes placed on the same plane modelled as capacitor *C1*, Conductance *G1* replicates the effects of dielectric loss and leakage through the substrate and the medium around it. This part manages the antenna's input impedance matching as well as making sure that the radiating modes are excited properly, the antenna's equivalent circuit model is created by combining two symmetrical T, and the horizontal arms of the both T's having the bend discontinuities, this T discontinuity stores electric energy, particularly near the junction area, due to fringing electric fields, which results in shunt capacitance. The horizontal arm of the T, which consists of the obtuse bend discontinuity used the 90^0 bend formulation, which requires tuning adjustments, and the gap between the horizontal arms gives rise to capacitance, modelled as shunt capacitor, due to the bend in the arm, the current direction changes suddenly, causing current crowding that increases magnetic field concentration. So, each bend contributes extra inductance, which is modelled as a series inductor in the equivalent circuit. The components values *L1*=2.02, *L2*=0.5, *L3*=1.2, *L4*=1.2, *L5*=1, *L6*=1, *L7*=1.5, *L8*=1.5, *L9*=1.5, *L10*=1, *L11*=1, *L12*= 1, *L13*=1, *L14*=0.5, *L15*=0.5, *R1*=28, *G1*=0.02 ʊ, *C1*=0.95, *C2*=9.71, *C3*=1, *C4*=1, *C5*=1, *C6*=0.9, *C7*=0.9 are calculated [12], as Inductor (*L*) in nH, Capacitor (*C*) in pF, Resistor (*R*) in Ω, Conductance (*G*) in ʊ.

$$L = \frac{1}{\omega^2 C} \tag{5}$$

$$R = \frac{Q}{\omega C} \tag{6}$$

Uncorrected Proof

10.22060/EEJ.2026.25667.5989

$$Q = \frac{C\sqrt{\varepsilon_e}}{4 f_r h} \tag{7}$$

$$C = \frac{\varepsilon_0 \varepsilon_e W h}{2h} \cos^{-2}\left(\frac{\pi S}{2L}\right) \tag{8}$$

$$\frac{C_b}{W}(\mathrm{pF/m}) = \left[\left(9.5\varepsilon_r + 1.25\right)\left(\frac{W}{h}\right) + 5.2\varepsilon_r + 7\right] \tag{9}$$

$$\frac{L_b}{h}(\mathrm{nH/m}) = 100\left(4\sqrt{\frac{W}{h}} - 4.21\right) \tag{10}$$

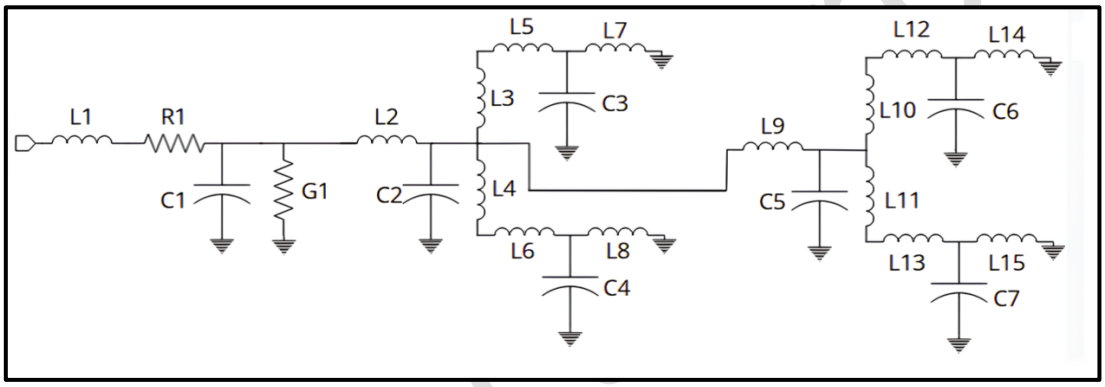


Fig. 7. The Equivalent Circuit of the Proposed Antenna

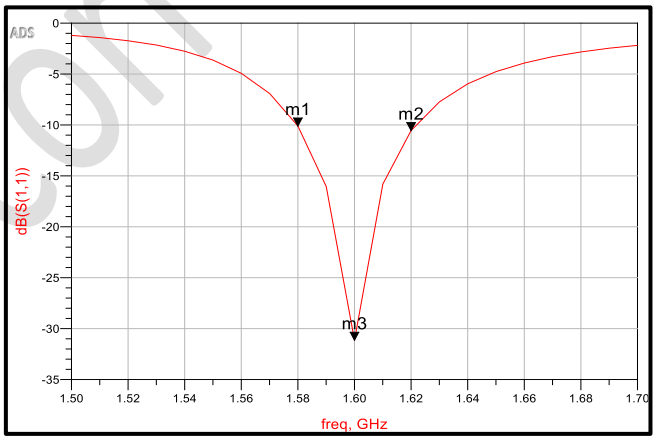


Fig. 8. Equivalent Circuit Model S_{11} Characteristic

4. Results and Discussions

Uncorrected Proof

10.22060/EEJ.2026.25667.5989

The fabricated prototype is used for testing with the help of Agilent N5247A: A.09.90.02 Vector Network Analyzer (VNA). Fig. 9 compares the measured reflection coefficient (S_{11}) results to those predicted by simulation. The physical displacement of the antenna during assembly slightly influences the measured results in terms of shift of frequency to 1.65 GHz from 1.6 GHz. Fig. 10 depicts a physical prototype of the antenna in a microwave electromagnetic anechoic chamber for the measurement of radiation pattern.

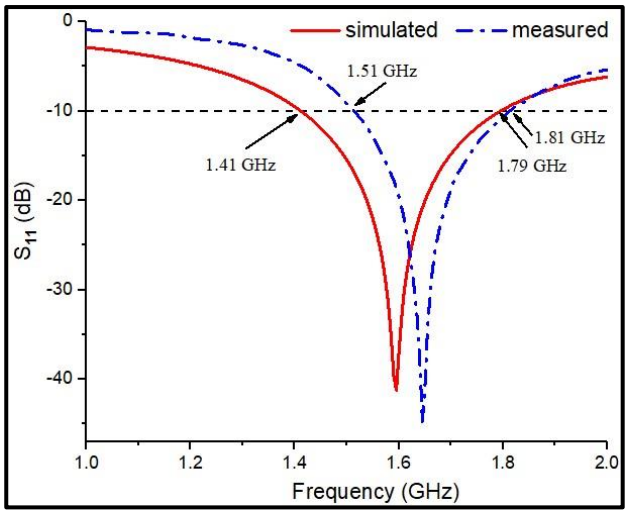
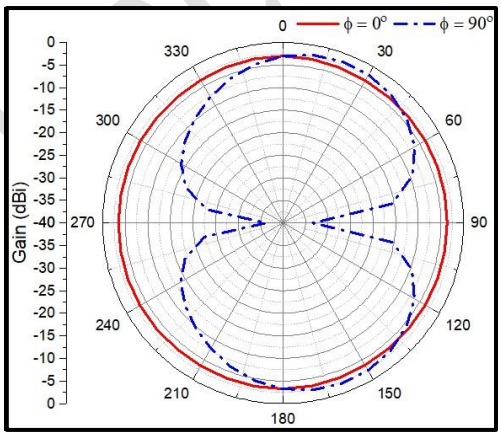


Fig. 9. Measured and Simulated S_{11}.

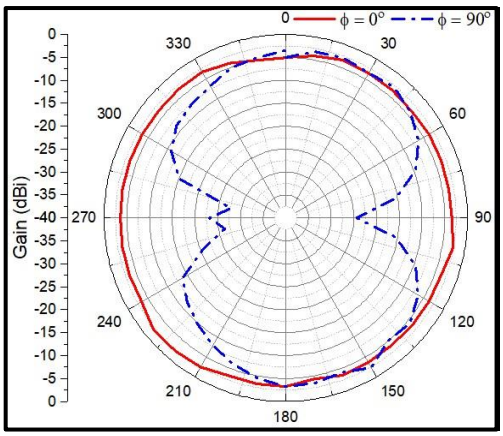


Fig. 10. Photograph of Anechoic Chamber Set up

Fig. 11 (a) and (b) shows the 2D radiation pattern of the proposed L-band wearable antenna, illustrating its gain distribution in two principal planes: $\phi=0^0$(red solid line) and $\phi=90^0$ (blue dashed line). The nearly omnidirectional pattern in the $\phi=0^0$ plane and the bidirectional characteristics in the $\phi=90^0$ plane demonstrates the antenna's suitability for body-centric communications, where consistent radiation in multiple directions is advantageous. The gain remained relatively stable across angles, with no deep nulls, supporting reliable signal coverage even under body movement and orientation changes. This radiation behaviour is particularly beneficial for wearable and on-body applications, ensuring robust connectivity in dynamic environments.



(a) Simulated

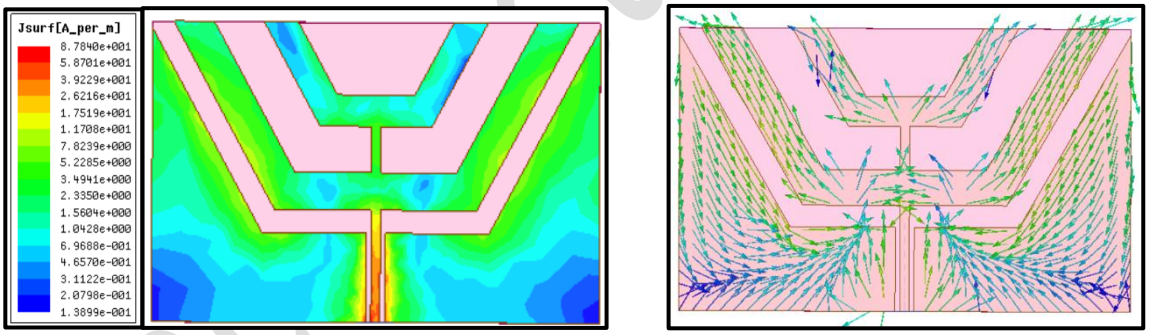


(b) Measured

Fig. 11. Radiation Pattern at 1.6 GHz

The surface current density distribution of the proposed CPW-fed half-hexagonal antenna illustrates a well-optimized current flow and efficient coupling between the feedline and radiating elements. A high concentration of current is observed at the CPW feed junction, where the signal transitions from the centre conductor to the radiating arms, confirming strong coupling and effective excitation. The symmetric dispersion of surface current along the angular arms ensures balanced radiation and supports linear polarization with minimal distortion. The smooth gradient from high (red/orange) to low (blue/green) current regions indicates good impedance matching, reduced back-reflection, and the absence of reactive hotspots. The planar nature of the CPW structure confines the electric and magnetic fields within the same layer, minimizing dielectric losses and surface wave propagation.

The current distribution of the proposed CPW-fed antenna in Fig. 12 illustrates a well-balanced and efficient radiation mechanism. The excitation originates at the central CPW feedline, where the signal propagates between the centre conductor and the adjacent coplanar ground planes. Surface currents flow symmetrically from the feed point into the radiating structure, particularly along the slanted and horizontal edges of the antenna geometry. As observed in the distribution plot, these current vectors diverge outward and upward, forming strong radiating paths that support efficient broadside radiation. The sloped arms guide the current smoothly, minimizing abrupt discontinuities and enhancing impedance matching. The absence of a backside ground plane and the planar nature of the CPW configuration help confine the electromagnetic fields within the substrate plane, effectively suppressing surface wave propagation and improving radiation efficiency. The symmetrical current flow further ensures low cross-polarization and stable far-field characteristics. Overall, the current behaviour confirms that the antenna operates effectively under planar excitation and is well-suited for compact, wideband, and flexible wireless applications.



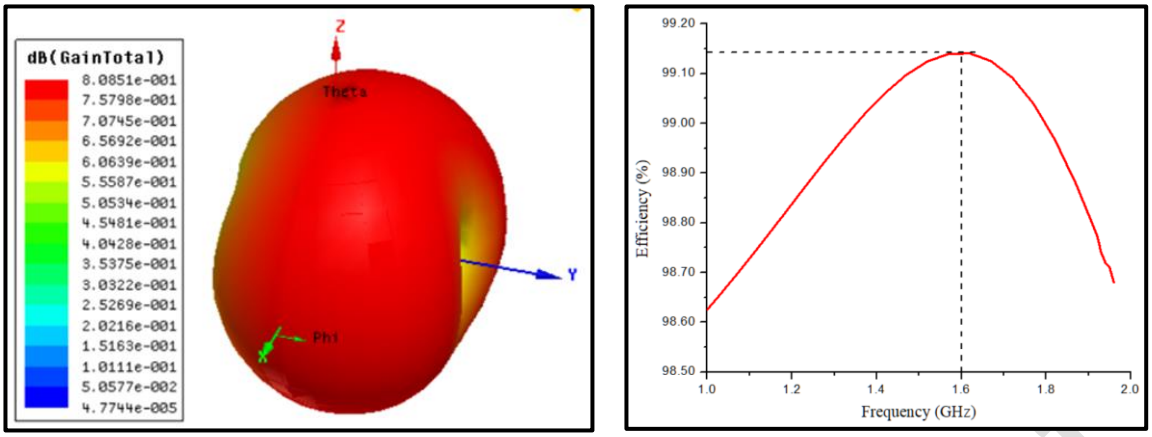
(a) Magnitude Form **(b) Vector Form**

Fig. 12. Current Distribution At 1.6 GHz

The total gain and radiation efficiency characteristics of the proposed antenna are shown in Figs. 13 (a) and (b). A distinct resonance is observed at 1.6 GHz, where the antenna achieves its maximum gain of approximately 0.8 dBi. The radiation efficiency reaches nearly 99.14% at the same frequency, indicating effective conversion of accepted power into radiated power. The gain and efficiency peaks demonstrate that the antenna operates efficiently at its designed resonant frequency and maintains stable radiation performance within the intended operating band.

Unformatted Proof

10.22060/EEJ.2026.25667.5989



(a) Gain **(b) Radiation efficiency**

Fig. 13. Gain and Radiation Efficiency Characteristics

5. Bending Analysis

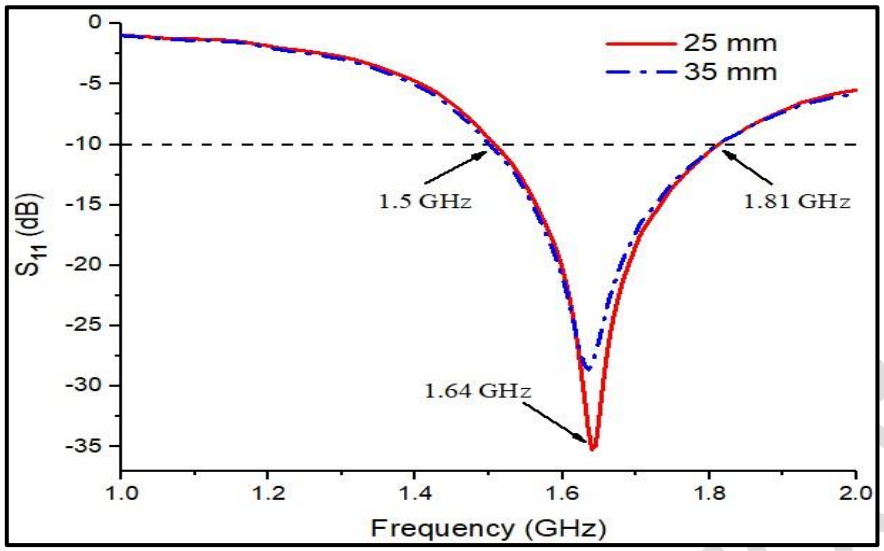
The bending performance of the proposed half-hexagonal L-band antenna is thoroughly investigated by conforming the structure to cylindrical PVC surfaces with radii of 25 mm and 35 mm, as illustrated in Fig. 14 (a). These configurations emulate practical wearable scenarios, such as mounting on limbs or curved surfaces, where mechanical deformation is inevitable. Bending the antenna alters the physical current distribution and modifies the effective dielectric loading, which in turn can affect the input impedance, resonance behavior, and radiation characteristics [23]. Despite these mechanical deformations, the antenna maintains a stable operational frequency near 1.6 GHz. Fig. 14 (b) illustrates that the reflection coefficient (S_{11}) remains below –10 dB throughout the L-band spectrum in both bending scenarios, suggesting that there is minimal detuning and good impedance matching. The observed frequency shift is marginal, attributed primarily to the change in effective permittivity and physical path length of surface currents.



(a)

Uncorrected Proof

10.22060/EEJ.2026.25667.5989



(b)

Fig. 14. Bending Analysis (a) Bending at 35 mm (b) S_{11} Comparison

Moreover, the antenna retains its wide impedance bandwidth, and the radiation pattern distortion is minimal, demonstrating the design's resilience to conformal stress. These results confirm that the current distribution remains sufficiently confined, and surface wave generation is suppressed due to the symmetric CPW feed and low-permittivity foam substrate. Overall, the bending analysis validates the antenna's mechanical robustness and electromagnetic stability, making it highly suitable for integration in flexible, wearable, and conformal L-band wireless systems.

The radiation pattern of the antenna was analyzed under flat, 35 mm bent, and 25 mm bent configurations. The bending introduces only minor variations in the radiation characteristics. As the bending radius decreases, slight changes in the surface current distribution and effective electrical length of the radiator occur, leading to small variations in main lobe. However, the overall radiation behavior remains largely unchanged. In both bent configurations, the antenna preserves its principal radiation direction and maintains stable radiation performance across the operating band. Although a slight reduction in peak gain and minor broadening of the main lobe are observed for the more severe bending condition (25 mm radius), no significant pattern distortion or beam tilting is detected. This demonstrates that the proposed antenna is capable of maintaining reliable radiation characteristics even under substantial mechanical deformation.

6. On-Body Analysis

The fabricated prototype is also tested on the body parts of the person who is 80 kg in weight and 5.8 ft. in height. The measurement is normally conducted on body parts like arm and chest as depicted in Figs. 15 (a) and (b). Furthermore, the antenna is tested on the flat surface of the arm near the wrist, as illustrated in Fig. 15 (c). The prototype has performed very well irrespective of size and posture of the body. The antenna is tuned to the frequency of 1.64 and 1.65 GHz for hand and chest respectively. A minor shift of resonating frequency is observed with body parts compared to designed frequency of 1.6 GHz. The matching is found very prominent with highest value around -40 and -42.5 dB respectively under the change of body part scenario. A comparison of S_{11} performance is presented in Fig. 15 (d) with the almost same bandwidth of 300 MHz for the hand and chest.

Unformatted Proof

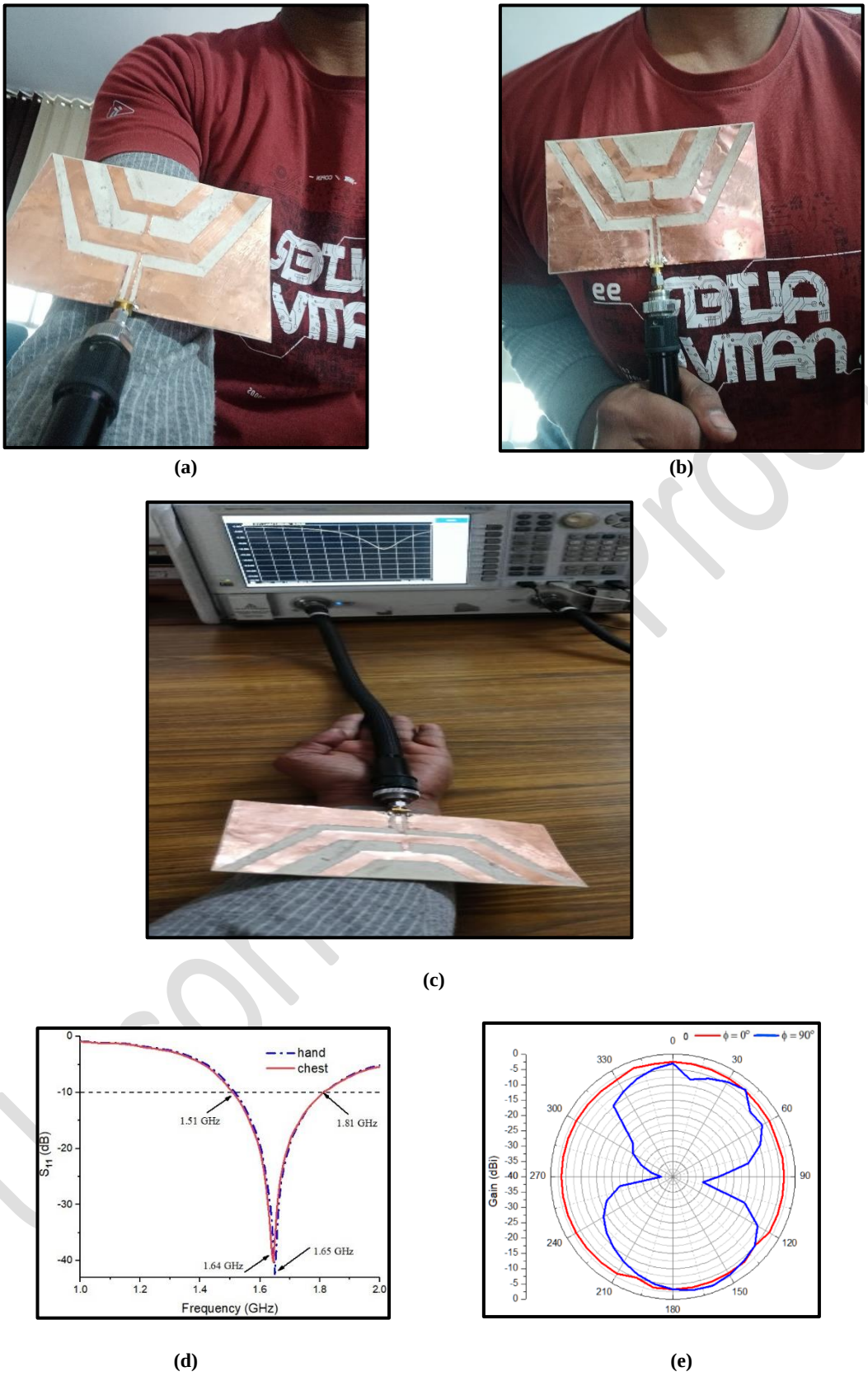


Fig. 15. On-body Analysis (a), (c) Arm (b) Chest (d) S_{11} Comparison (e) Radiation Pattern for Chest Position

Fig. 15 (e) indicates that the presence of body tissues slightly modifies the radiation characteristics due to the lossy and high-permittivity nature of the human body. A reduction in radiation intensity is observed in the direction facing the body because part of the radiated energy is absorbed by the surrounding tissues. Consequently, a slight decrease in peak gain is noted under on-body conditions. Despite these effects, the antenna maintains its overall radiation characteristics, and the main radiation direction remains substantially unchanged. However, no significant pattern distortion or beam tilting occurs. The stable radiation behavior demonstrates that the proposed antenna can operate effectively in close proximity to the human body.

7. SAR Analysis

Wearable antennas function in close proximity to the human body, which is inherently lossy, influencing their operational efficiency, impedance matching, bandwidth, and gain. When electromagnetic waves propagate, a fraction of the emitted radiation interacts with the body, penetrating the skin and being absorbed. This phenomenon raises health concerns due to potential biological effects. Apart from enduring mechanical deformations such as bending and crumpling, wearable antennas must exhibit superior efficiency while adhering to stringent specific absorption rate (SAR) constraints. SAR represents the power absorbed per unit mass of biological tissue, measured in W/kg. Recognizing its critical implications, various regulatory authorities have imposed stringent SAR limits to ensure user safety. SAR is typically measured using either simulations or physical models of the human body, with absorption assessed over tissue volumes of 1 gram (1 g) or 10 grams (10 g). The 1 g SAR captures the highest average energy absorption within a small tissue area, reflecting localized energy concentration, while the 10 g SAR provides an average absorption over a larger tissue volume, offering a more general view of overall exposure. Safety regulations for SAR are usually based on these measurements, with stricter limits applied to the 1 g SAR in smaller, more concentrated tissue regions [24-28].

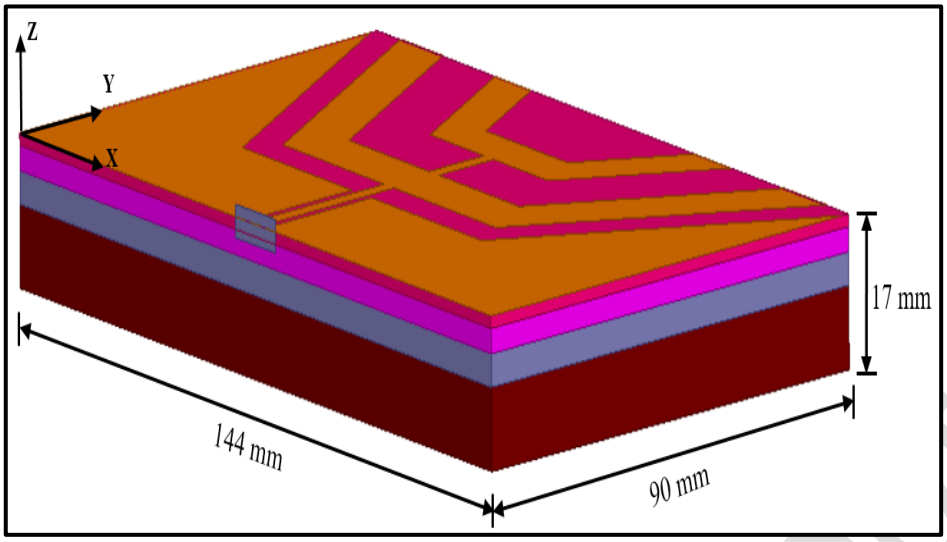
To elegantly assess the SAR characteristics of the proposed half hexagonal antenna, a comprehensive analysis is carried out for both on-body and off-body scenarios at varying distances. A meticulously constructed three-layer human body phantom is developed in HFSS, operating at 1.6 GHz, to emulate the skin, fat, and muscle tissues. The thicknesses of these layers were precisely defined as 3 mm, 4 mm, and 10 mm, respectively [29-32]. The corresponding electrical properties are detailed in Table 4, while Fig. 16 (a) visually presents the constructed phantom model enriched with these parameters. An excitation power of 1 mW is applied to the antenna to examine the Specific Absorption Rate (SAR) within 1-gram and 10-gram tissue volumes. The simulation of the antenna in proximity to the phantom allowed for accurate SAR evaluation, providing valuable insight into the electromagnetic interaction with biological tissues. The SAR values obtained from the on-body analysis are effectively presented in Figs. 16 (b) and (c).

Table 4. Electrical Properties of Human Tissues at 1.6 GHz [33-35]

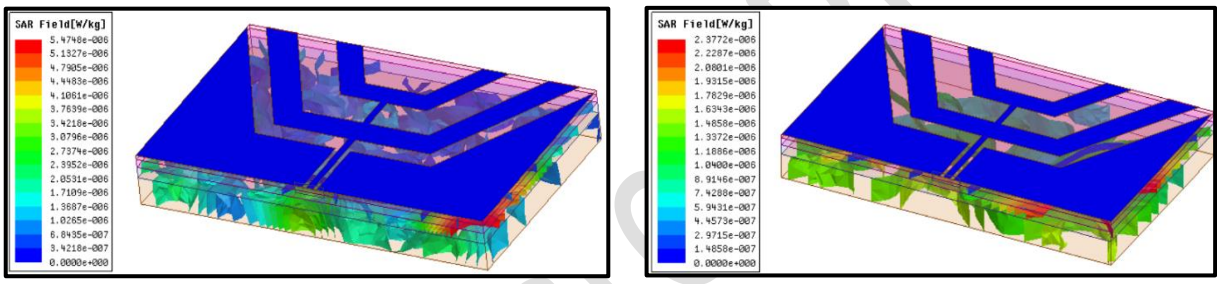
Tissue / Parameter	Frequency (GHz)	Conductivity σ (S/m)	Permittivity (ε_r)	Loss tangent	Mass density (Kg/m^3)
Skin		1.11	39.22	0.3174	1109
Fat	1.6	0.071	5.37	0.17186	911
Muscle		1.23	53.82	0.25818	1090

Uncorrected Proof

10.22060/EEJ.2026.25667.5989



(a)

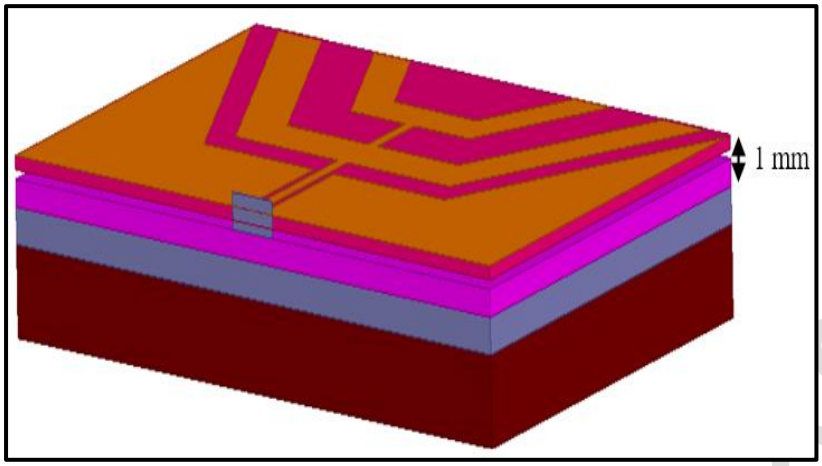


(b) **(c)**

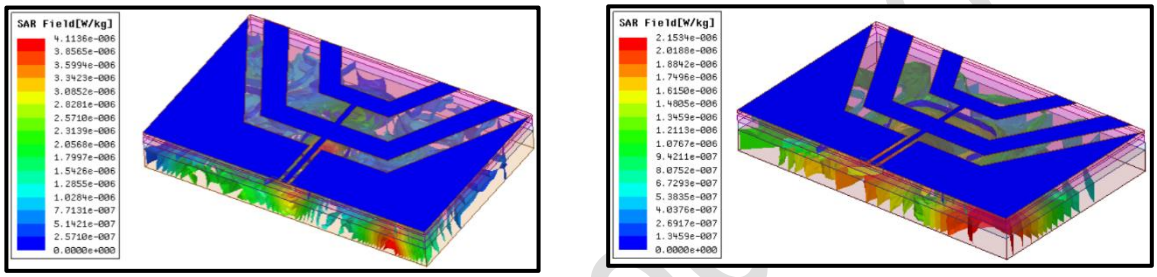
Fig. 16. (a) Three-Layer Body Phantom for SAR Analysis (b) SAR at 1 gram (c) SAR at 10 gram

For the on-body arrangement, the computed SAR values for 1-gram and 10-gram tissue masses are 5.474µW/kg and 2.377µW/kg, respectively. To investigate the spatial variation of SAR, the same multilayer phantom setup is employed for off-body conditions. A tissue-equivalent human body phantom is strategically positioned in proximity to the RF source to replicate realistic electromagnetic exposure. SAR simulations are performed to quantify the power absorption within the phantom at specified spatial separations. At a separation of 1 mm from the phantom surface, a distinct variation in SAR distribution is observed for both tissue masses, as illustrated in Fig. 17 (a). The SAR values at this offset distance are calculated to be 4.113µW/kg for 1-gram tissue and 2.153µW/kg for 10-gram tissue, as depicted in Figs. 17(b) and 17(c) respectively.

Uncorrected Proof



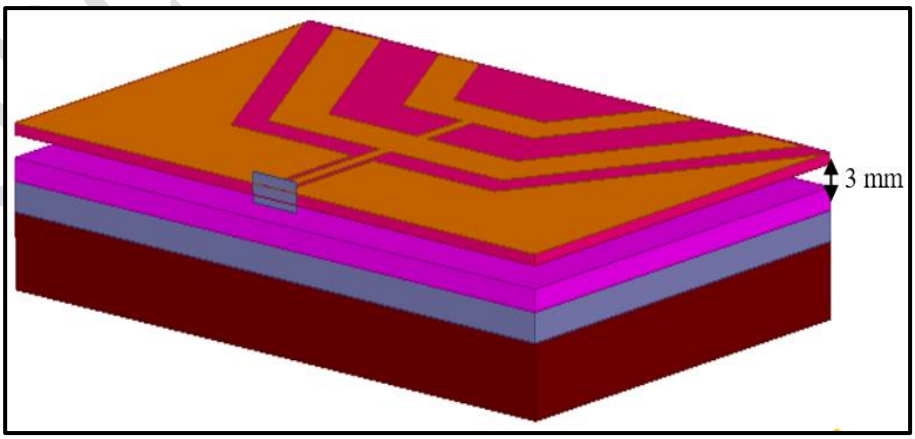
(a)



(b) **(c)**

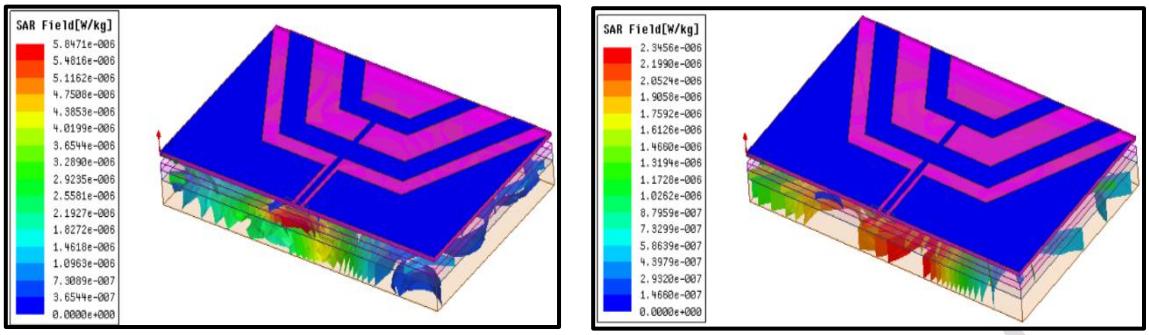
Fig. 17. (a) SAR Analysis for 1 mm away from the Body (b) 1 gram (c) 10 gram

Similarly, SAR analysis is performed with the antenna positioned 3 mm away from the body phantom. The phantom model formed at this separation is shown in Fig. 18(a), while Figs. 18(b) and 18(c) illustrate the corresponding SAR distributions and electromagnetic wave penetration across the three-layer tissue model for 1-gram and 10-gram tissues, respectively. The maximum SAR values observed in this arrangement are 5.847μW/kg for 1 gram and 2.345 μW/kg for 10 grams of tissue.



(a)

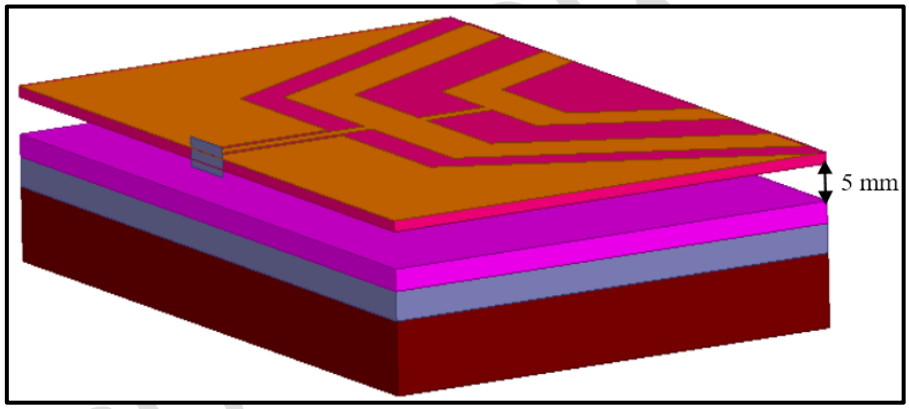
Uncorrected Proof



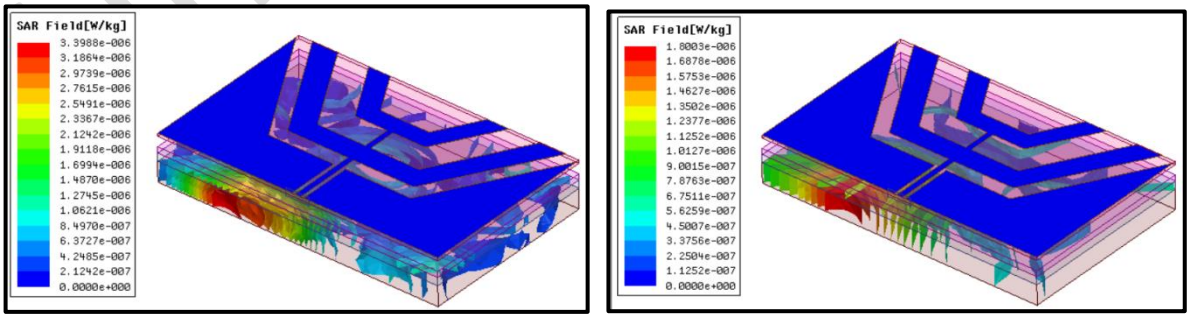
(b) **(c)**

Fig. 18. (a) SAR Analysis at 3 mm away from the Body (b) 1 gram (c) 10 gram

In addition, SAR evaluation is carried out with the antenna positioned 5 mm away from the body phantom. Fig. 19(a) displays the phantom setup at this separation, while Figs. 19(b) and (c) illustrate the resulting SAR distribution and electromagnetic field interaction within 1-gram and 10-gram tissue samples, respectively. The peak SAR values at this distance are measured as 3.398 µW/kg for 1 gram and 1.800 µW/kg for 10 grams of tissue.



(a)



(b) **(c)**

Fig. 19. (a) SAR Analysis at 5 mm away from the Body (b) 1 gram (c) 10 gram

10.22060/EEJ.2026.25667.5989

A comprehensive summary of SAR results for all tested conditions including on-body, 1 mm, 3 mm, and 5 mm distance is provided in Table 5. The simulation results reveal a clear downward trend in SAR values as the distance between the RF source and the body phantom increases. This reduction aligns with the inverse square law, which states that electromagnetic power density diminishes proportionally to the square of the distance from the source. As a result, energy absorption by biological tissues is significantly reduced at greater distances, leading to lower SAR levels. Overall, it is concluded that the proposed half hexagonal antenna remains safe under all evaluated configurations. Whether placed directly on the body or positioned at a distance, the measured SAR values consistently fall well below the internationally accepted safety limits of 1.6 W/kg for 1-gram and 2 W/kg for 10-gram tissue, confirming its compliance with electromagnetic exposure guidelines.

Table 5. Summary of SAR Results

SAR	1 gram (µW/kg)	10 grams (µW/kg)
On-body	5.474	2.377
1 mm away	4.113	2.153
3 mm away	5.847	2.345
5 mm away	3.398	1.800

Additionally, a SAR analysis with the 1W input power is performed for 1-gram and 10-gram tissue in order to realize the impact of practical consideration of the proposed antenna. This is accomplished by exciting the antenna with the new input power of 1W. The results obtained for the 1W input power are presented in Figs. 20 (a) and (b). When 1W input power is applied for SAR analysis then 4.747 µW/kg of 1mW input power is converted to 4.747 mW/kg; this shows that the lower value of SAR is possible with the lower value of dielectric constant for the substrate material used. A generalized normalization formula can be used for the conversion of the change of input power as stated in Eq. (11)

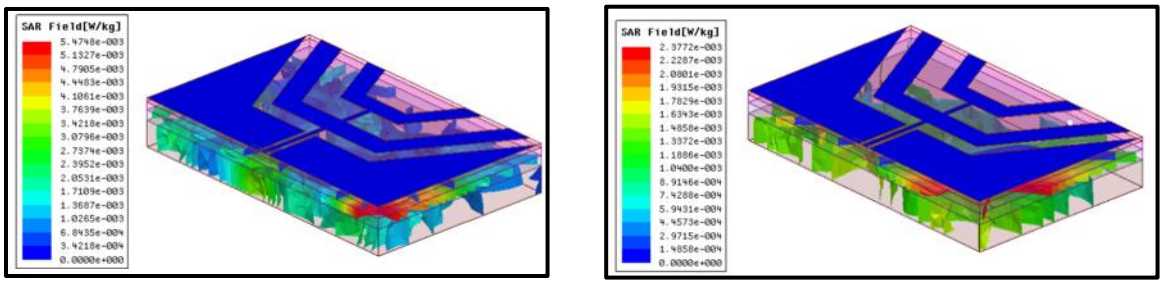
$$SAR_{new} = SAR_{1mw} \times \frac{P_{new}}{1\text{mw}} \tag{11}$$

Where SAR_{1mW} is the SAR obtained at 1 mW input power and P_{new} is the desired operating power. For example, if the maximum reported SAR is 4.747 µW/kg at 1 mW, the corresponding SAR at 1W would be as in Eq. (12)

$$4.747\mu \times 1000 = 4.747\text{mW / Kg} \tag{12}$$

The SAR values scaled to practical operating powers typically used in wireless body-area and wearable communication systems (e.g. 1W). Even under these conditions, the SAR values remain within the limits specified by the regulatory guidelines of the Federal Communications Commission (1.6 W/kg averaged over 1g tissue) and International Commission on Non-Ionizing Radiation Protection (2 W/kg averaged over 10 g tissue).

Uncorrected Proof



(a) 1 gram **(b) 10 gram**

Fig. 20. SAR Analysis with 1W Input Power

The results of the proposed antenna are compared with earlier work for the necessary parameters of L band wearable antenna in the Table 6.

Table 6. Comparison of Proposed Antenna with Earlier Work

Ref.	Size (mm)	Bandwidth (MHz)	Gain (dBi)	Efficiency (%)	SAR (W/kg)
[2]	70 x 45	40.5	3.47	97	--
[36]	85 x 77	56	1.02	----	0.168
[37]	25 x 25	40	3.15	>85	--
[38]	35 x 36	---	1.3	70-75	--
[39]	172 x 96	39	4.39	---	--
This work	90 x 144	383	-3.72	99.14	5.474µ @ 1g 2.377µ @10g

8. Conclusion

A CPW-fed L-band antenna has been efficiently designed and optimized for wearable communication systems, with a focus on achieving compactness, high performance, and user safety. The final design, based on a fractal geometry derived from a modified half-hexagonal structure, successfully resonates at 1.6 GHz, precisely within the L-band spectrum. This fractal approach enhanced the antenna's electromagnetic behavior, resulting in excellent impedance matching with a S_{11} value of –41.25 dB and a substantial bandwidth of 383 MHz. These parameters ensure reliable and efficient signal transmission, which is critical for applications such as health monitoring and wireless body area networks (WBANs). Also, the proposed antenna has achieved drastic size reduction to 50 %. To evaluate real-world usability, the antenna underwent extensive on-body and bending analysis. The results demonstrated consistent performance under various bending scenarios, confirming the antenna's mechanical flexibility and electromagnetic stability when worn on curved surfaces such as arms and legs. Furthermore, SAR analysis was conducted using a multilayer tissue phantom model over the body and 1mm, 3 mm and 5 mm away to assess user safety. The SAR values were found to be well within the acceptable limits, ensuring safe operation when in close contact with human skin. Overall, the proposed antenna design offers an ideal solution for next-generation wearable devices operating within the L-band.

9. Declarations

Uncorrected Proof

Availability of data and material
The datasets generated and/or analysed during the current study are not publicly available due to research work but are available from the corresponding author on reasonable request.

Competing interests
The authors declare that they have no competing interests.

Funding
The authors declare that they have not received any grant or funding for this research work by state, national or international agency, institute and or industry.

10. LIST OF ABBREVIATIONS

dB	Decibel
E	electric field in rms $V.m^{-1}$
ε	Permittivity (F/m)
f	Feed
FBW	Fractional bandwidth
FCC	Federal Communications Commission
g	Ground
GHz	Gigahertz
ICNIRP	International Commission on Non-Ionizing Radiation Protection
IEEE	Institute of Electrical and Electronics Engineers
kg	Kilogram
L	Length, in mm
L_{SI}	Inner slot legnth in mm
L_{SL}	Slot legnth
L_{SO}	Outer slot legnth
M	Megahertz
mm	Millimeter
r	relative
S	Scattering
S_{11}	return loss
SAR	Specific Absorption Rate
sub	Substrate
W	Width, in mm
W/kg	Watt per kilogram
W_{SL}	Slot width, in mm
ρ	density of sample $kg.m^{-3}$
σ	conductivity of sample, $S.m^{-1}$

Uncorrected Proof

References

[1] S. Kumar, R. Khandekar, and P. Tupe-Waghmare, "Frequency reconfigurable patch antenna for L-band applications," International Journal of Engineering and Advanced Technology, vol. 9, no. 1, pp. 4775–4784, 2019.

[2] A. Kiran, G. K. Mishra, S. Kumar, S. Kumar, and R. Prasad, "Wearable textile antenna for GPS application," in Proc. 27th International Symposium on Wireless Personal Multimedia Communications (WPMC), Greater Noida, India, pp. 1–4, 2024.

[3] M. J. Ammann, and A. Alomainy, "Antennas and propagation for body-centric wireless communications," IEEE Antennas and Propagation Magazine, vol. 54, no. 5, pp. 116–122, 2012.

[4] S. M. Ali, C. Sovuthy, M. A. Imran, S. Socheatra, Q. H. Abbasi, and Z. Z. Abidin, "Recent advances of wearable antennas in materials, fabrication methods, designs, and their applications: State-of-the-art," Micromachines, vol. 11, no. 10, Art. no. 888, 2020.

[5] RF Wireless World, "RF Wireless World." [Online]. Available: https://www.rfwireless-world.com.

[6] N. M. Sarmad et al., "Recent advances in wearable antenna technologies: A review," Progress in Electromagnetics Research B, vol. 89, pp. 1–27, 2020.

[7] R. Li, and M. M. Tentzeris, "Wearable antennas for body area networks," IEEE Microwave Magazine, vol. 10, no. 1, pp. 92–99, 2006.

[8] K. N. Paracha, S. K. Abdul Rahim, P. J. Soh, and M. Khalily, "Wearable antennas: A review of materials, structures, and innovative features for autonomous communication and sensing," IEEE Access, vol. 7, pp. 56694–56712, 2019.

[9] H. Sun, Z. Zhang, R. Q. Hu, and Y. Qian, "Wearable communications in 5G: Challenges and enabling technologies," IEEE Vehicular Technology Magazine, vol. 13, no. 3, pp. 100–109, 2018.

[10] A. Alomainy, and Y. Hao, "Modeling and characterization of textile antennas for wearable applications," IEEE Transactions on Antennas and Propagation, vol. 55, no. 4, pp. 1332–1340, 2007.

[11] P. Salonen, and Y. Rahmat-Samii, "Textile antennas: Effects of antenna bending on input matching and impedance bandwidth," IEEE Aerospace and Electronic Systems Magazine, vol. 22, no. 12, pp. 18–22, 2007.

[12] R. Garg, P. Bhartia, I. Bahl, and A. Ittipiboon, "Microstrip Antenna Design Handbook," Norwood, MA, USA: Artech House, 2001.

[13] B. Bhartia, and I. J. Bahl, "Microstrip Antennas," Artech House, 1980.

[14] T. Huynh, and K. F. Lee, "Single-layer single-patch wideband microstrip antenna," Electronics Letters, vol. 31, no. 16, pp. 1310–1312, 1995.

[15] R. Chair, K. F. Lee, C. L. Mak, K. M. Luk, and A. A. Kishk, "Miniature wideband half U-slot and half E-patch antennas," IEEE Transactions on Antennas and Propagation, vol. 53, no. 8, pp. 2645–2652, 2005.

Uncorrected Proof

[16] A. A. Deshmukh, and G. Kumar, "Various slot-loaded broadband and compact circular microstrip antennas," Microwave and Optical Technology Letters, vol. 48, no. 3, pp. 435–439, 2006.

[17] V. Saidulu, "Design inset-fed microstrip patch antenna for L-band applications," International Journal of Innovative Technology and Exploring Engineering, vol. 10, no. 5, pp. 4–7, 2021.

[18] M. Latrach, and S. Islam, "Small broadband patch antenna design for L-band applications," in Proc. 32nd URSI General Assembly and Scientific Symposium (URSI GASS), Montreal, Canada, Aug. 19–26, 2017.

[19] A. S. Prabowo, N. Pambudiyatno, and B. B. Harianto, "Microstrip antenna design with rectangular patch for primary surveillance radar (PSR) L-band application," Journal of Physics: Conference Series, vol. 1845, no. 1, Art. no. 012033, 2021.

[20] A. Hajiaboli, F. Hodjat Kashani, and M. Omidi, "Broadband stacked microstrip patch antenna for L-band operation: FDTD Modeling," Iranian Journal of Electrical and Electronic Engineering, vol. 3, no. 3, pp. 64-71, 2007.

[21] C. A. Balanis, "Antenna Theory: Analysis and Design," 4th edition, Hoboken, NJ: USA, John Wiley & Sons, 2016.

[22] K. V. Karad, and V. S. Hendre, "A hexagonal-shape fractal flexible UWB antenna based on jeans material for healthcare applications," The Journal of The Textile Institute, vol. 116, no. 7, pp. 1227–1242, 2024.

[23] K. V. Karad, and V. S. Hendre, "A foam-based compact flexible wideband antenna for healthcare applications," Progress in Electromagnetics Research C, vol. 123, pp. 197–212, 2022.

[24] L. Corchia, G. Monti, E. De Benedetto, and L. Tarricone, "Wearable antennas for remote health care monitoring systems," International Journal of Antennas and Propagation, vol. 2017, pp. 1–11, 2017.

[25] K. V. T. R. Rao, "Estimation of specific absorption rate using infrared thermography for the biocompatibility of wearable wireless devices," Progress in Electromagnetics Research M, vol. 56, pp. 101–109, 2017.

[26] S. J. Priyadarshini, and D. Hemanth, "Investigation and reduction methods of specific absorption rate for biomedical applications: A survey," International Journal of RF and Microwave Computer-Aided Engineering, vol. 28, no. 3, pp. 1–15, 2018.

[27] J. P. Stephen, and D. J. Hemanth, "An investigation on specific absorption rate reduction materials with human tissue cube for biomedical applications," International Journal of RF and Microwave Computer-Aided Engineering, vol. 29, no.12, pp. 1-19, 2019.

[28] "What is SAR?" Everything RF, Feb. 21, 2019. [Online]. Available: https://www.everythingrf.com/community/what-is-sar.

[29] S. Doddipalli, A. Kothari, and P. Peshwe, "A low-profile ultrawideband monopole antenna for wearable applications," International Journal of Antennas and Propagation, vol. 2017, pp. 1-9, 2017.

[30] K. V. Karad, and V. S. Hendre, "A flower bud-shaped flexible UWB antenna for healthcare applications," Journal of Wireless Communications and Networking, vol. 2023, Art. no. 27, 2023.

Uncorrected Proof

[31] Mengjun Wang, Ze Yang, Jianfei Wu, Jianhui Bao, Jianying Liu, Lulu Cai, Tao Dang, Hongxing Zheng, and Erping Li, "Investigation of SAR reduction using flexible antenna with metamaterial structure in wireless body area network," IEEE Transactions on Antennas and Propagation, vol. 66, no. 6, pp. 3076–3086, 2018.

[32] Usman Ali, Ullah Sadiq, Khan Jalal, Shafi Muhammad, Kamal Babar, Basir Abdul, Flint James A, and R. D. Seager, "Design and SAR analysis of wearable antenna on various parts of human body, using conventional and artificial ground planes," Journal of Electrical Engineering and Technology, vol. 12, no. 1, pp. 317–328, 2017.

[33] International Commission on Non-Ionizing Radiation Protection (ICNIRP), "Guidelines for limiting exposure to electromagnetic fields (100 kHz to 300 GHz)," Health Physics, vol. 118, no. 5, pp. 483–524, 2020.

[34] "Dielectric Properties of Body Tissues: HTML clients," IFAC-CNR. [Online]. Available: http://niremf.ifac.cnr.it/tissprop/htmlclie/htmlclie.php.

[35] P.A. Hasgall, E Neufeld, M.C. Gosselin, A. Klingenbock, N Kuster, and N Kuster, "IT'IS Database for thermal and electromagnetic parameters of biological tissues," version 4.1, 2012.

[36] Yoshi Magdalena, Radial Anwar, Yuyu Wahyu, Mohamad Ismail Sulaiman, Zuhanis Mansor, and Dwi Andi Nurmantris, "Performance comparison of cotton and silk substrates on 1.575 GHz frequency textile antenna," Elektronika ir Elektrotechnika, vol. 27, no. 5, pp. 26-33, 2021.

[37] Prutha Kulkarni, and Raju Srinivasan, "Compact polarization diversity patch antenna in L and WiMAX bands for IoT applications," AEÜ – International Journal of Electronics and Communications, vol. 136, Art. no. 153772, 2021.

[38] Sangeetha Subbaraj, Manimala K., Subhagar S., Nandha Kumar R., Daanish Azim Sheikh, and Chandru S. M., "Performance enhanced compact multiband antenna for smartwatch applications," Microwave and Optical Technology Letters, vol. 68, no. 2, pp. 1-12, 2026.

[39] S. Mishra, S. Das, S. S. Pattnaik, S. Kumar, and B. K. Kanaujia, "Low-profile circularly polarized planar antenna for GPS L1, L2, and L5 bands," Microwave and Optical Technology Letters, vol. 62, no. 2, pp. 806–815, 2020.

Uncorrected Proof